Supplementary information for

# Molecular insights into the α6β4 nicotinic acetylcholine receptor function and ligand recognition

This document contains supplementary Figures 1-10 and Supplementary Tables 1-2

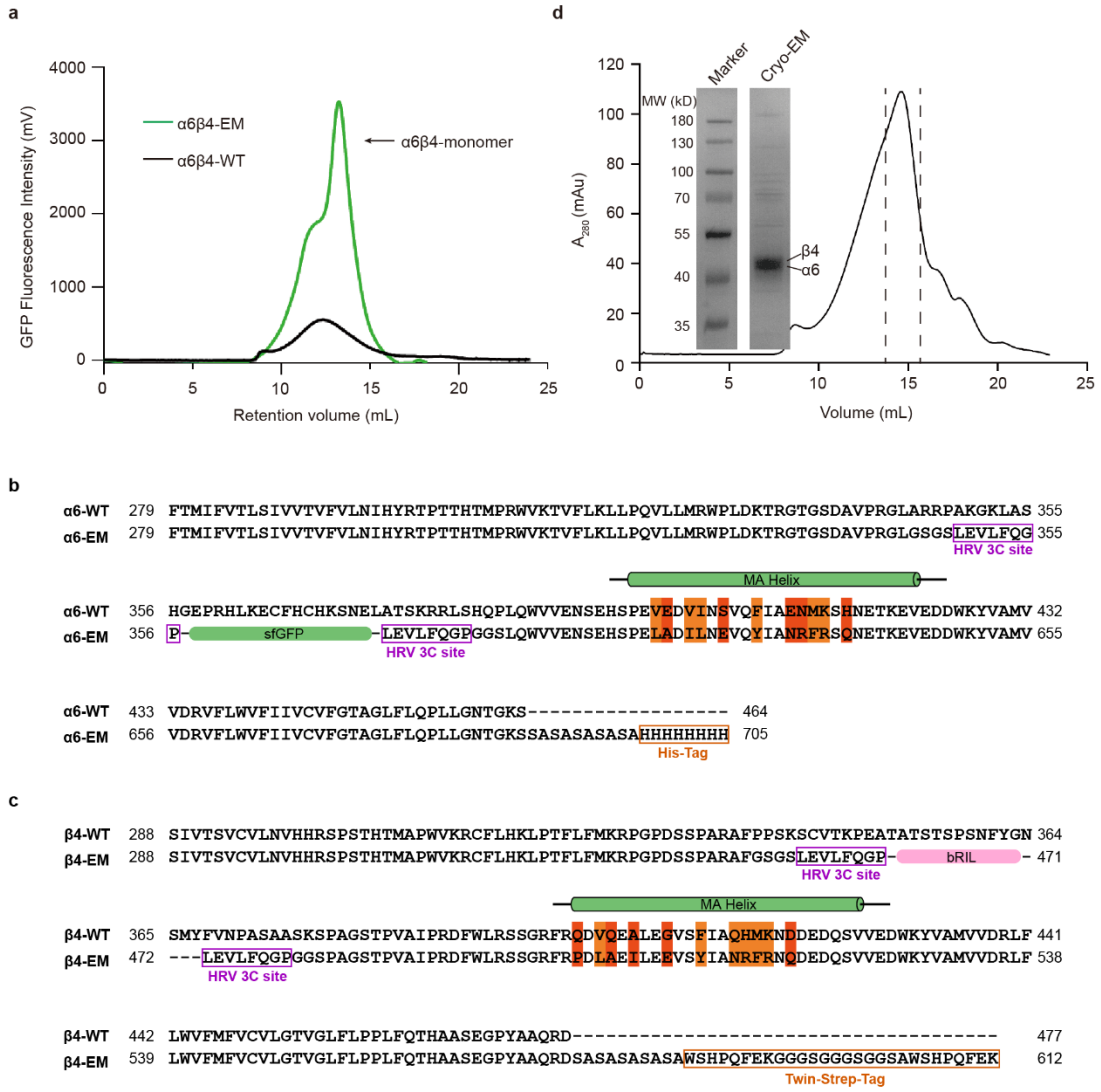


## Supplementary Fig 1. Construct optimization and protein purification

**a.** Comparison of protein samples of the wild-type (WT) α6β4 and EM α6β4 used to solve the α6β4 structures by FSEC. The curves of WT α6β4 and EM α6β4 are colored black and green, respectively. **b.** Alignment of mature coding sequences of WT human α6 subunit and EM α6 subunit constructs. The MA helix boundary is indicated by a green cylinder. The GFP sequence is represented by a green elliptical shape. The sequences of HRV-3C protease cleavage site and his-tag are labeled by purple and yellow dashes. **c.** Alignment of mature coding sequences of WT human β4 subunit and EM β4 subunit constructs. The MA helix boundary is indicated by a green cylinder. The bRIL sequence is represented by a pink elliptical shape. The sequences of HRV-3C protease cleavage site and twin-strep-tag are labeled by purple and yellow dashes. **d.** Representative profile of the α6β4 proteins by chromatogram (Superose 6 increase). Peak fraction (marked by black dashed lines) of α6β4 were pooled and concentrated cryo-EM study. SDS-PAGE gel of the α6β4 cryo-EM sample stained with Coomassie blue, and the bands of α6 and β4 subunits are labeled. The experiments are repeated independently for more than 3 times with similar results.

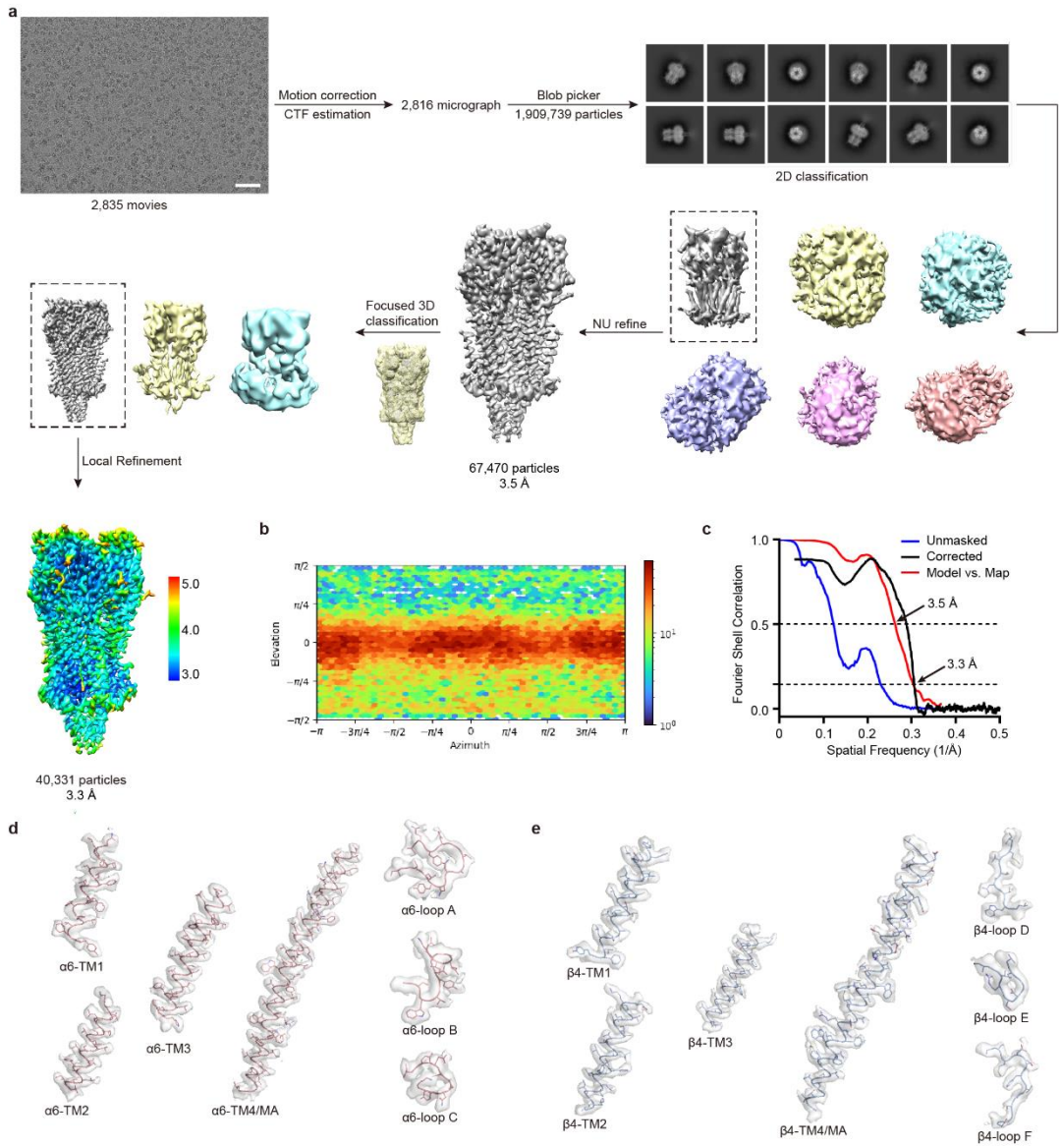


## Supplementary Fig 2. Cryo-EM data analysis of the α6β4$^{nico}$ receptor

**a.** Flowchart for cryo-EM data processing of α6β4 receptor bound with nicotine. A representative raw cryo-EM micrograph is shown here (Bar=50 nm). Particles were cleaned using multiple rounds of classifications. The final map was reported at 3.3 Å according to GSFSC criterion. The sharpened map of α6β4 receptor colored according to the estimated value of local resolution. **b.** Angular sampling of the final reconstruction, illustrating the orientation distribution of particles in the final reconstruction of α6β4$^{nico}$. **c.** *Fourier* shell correlations (FSC) curves of the α6β4 receptor and its atomic model. The unmasked (blue) and masked (red) FSC curves were calculated between two independently refined half-maps before and after map sharpening. The model-vs-map FSC (black) was calculated between the full map and the atomic model. **d.** The cryo-EM densities and atomic models of TM1-4, MA helix, loop A-C of α6. **e.** The cryo-EM densities and atomic models of TM1-4, MA helix, loop D-F of β4.

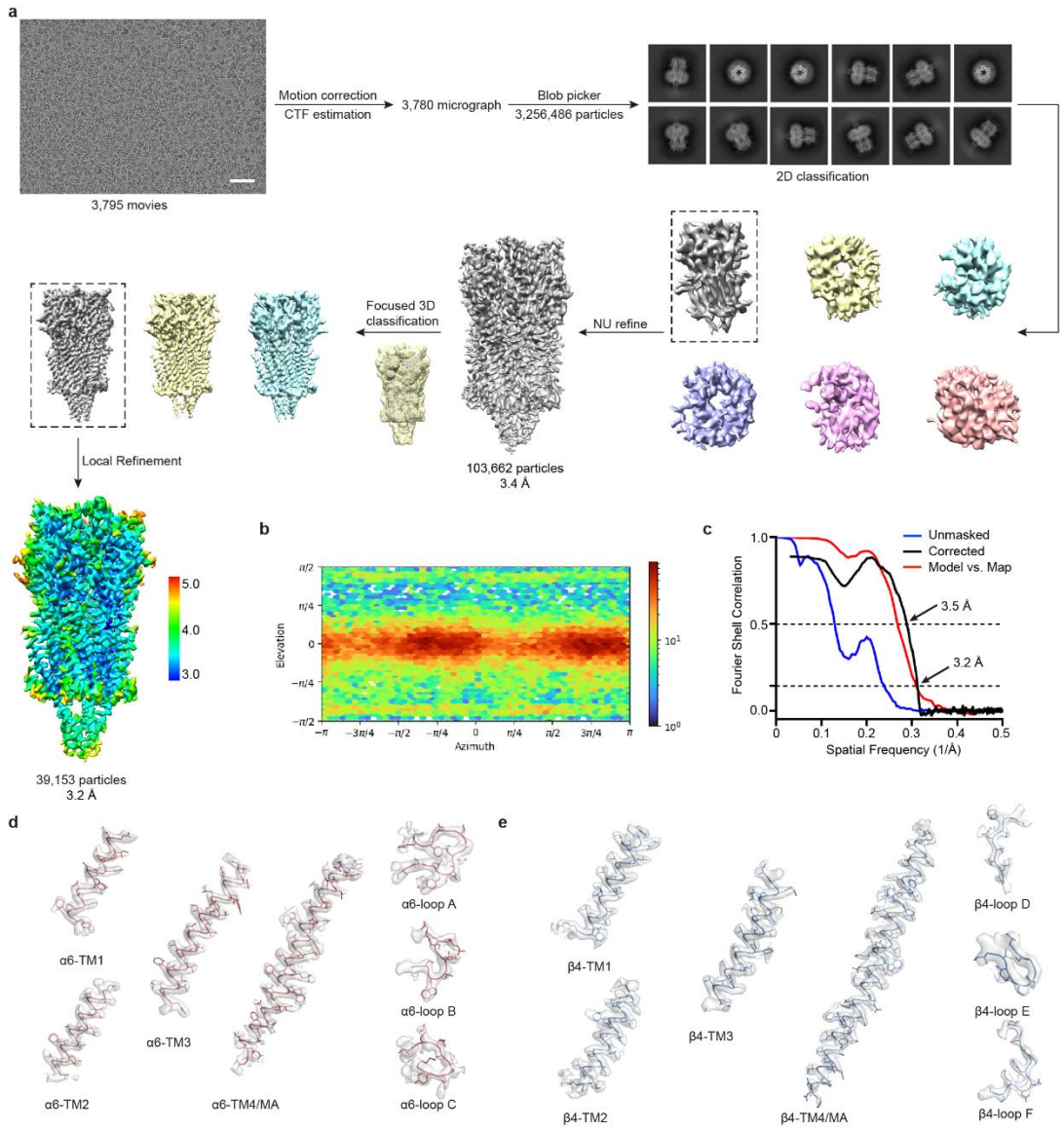


## Supplementary Fig 3. Cryo-EM data analysis of the α6β4$^{teb}$ receptor

**a.** Flowchart for cryo-EM data processing of α6β4 receptor bound with tebanicline. A representative raw cryo-EM micrograph is shown here (Bar=50 nm). Particles were cleaned using multiple rounds of classifications. The final map was reported at 3.2 Å according to GSFSC criterion. The sharpened map of α6β4 receptor colored according to the estimated value of local resolution. **b.** Angular sampling of the final reconstruction, illustrating the orientation distribution of particles in the final reconstruction of α6β4$^{teb}$. **c.** *Fourier* shell correlations (FSC) curves of the α6β4 receptor and its atomic model. The unmasked (blue) and masked (red) FSC curves were calculated between two independently refined half-maps before and after map sharpening. The model-vs-map FSC (black) was calculated between the full map and the atomic model. **d.** The cryo-EM densities and atomic models of TM1-4, MA helix, loop A-C of α6. **e.** The cryo-EM densities and atomic models of TM1-4, MA helix, loop D-F of β4.

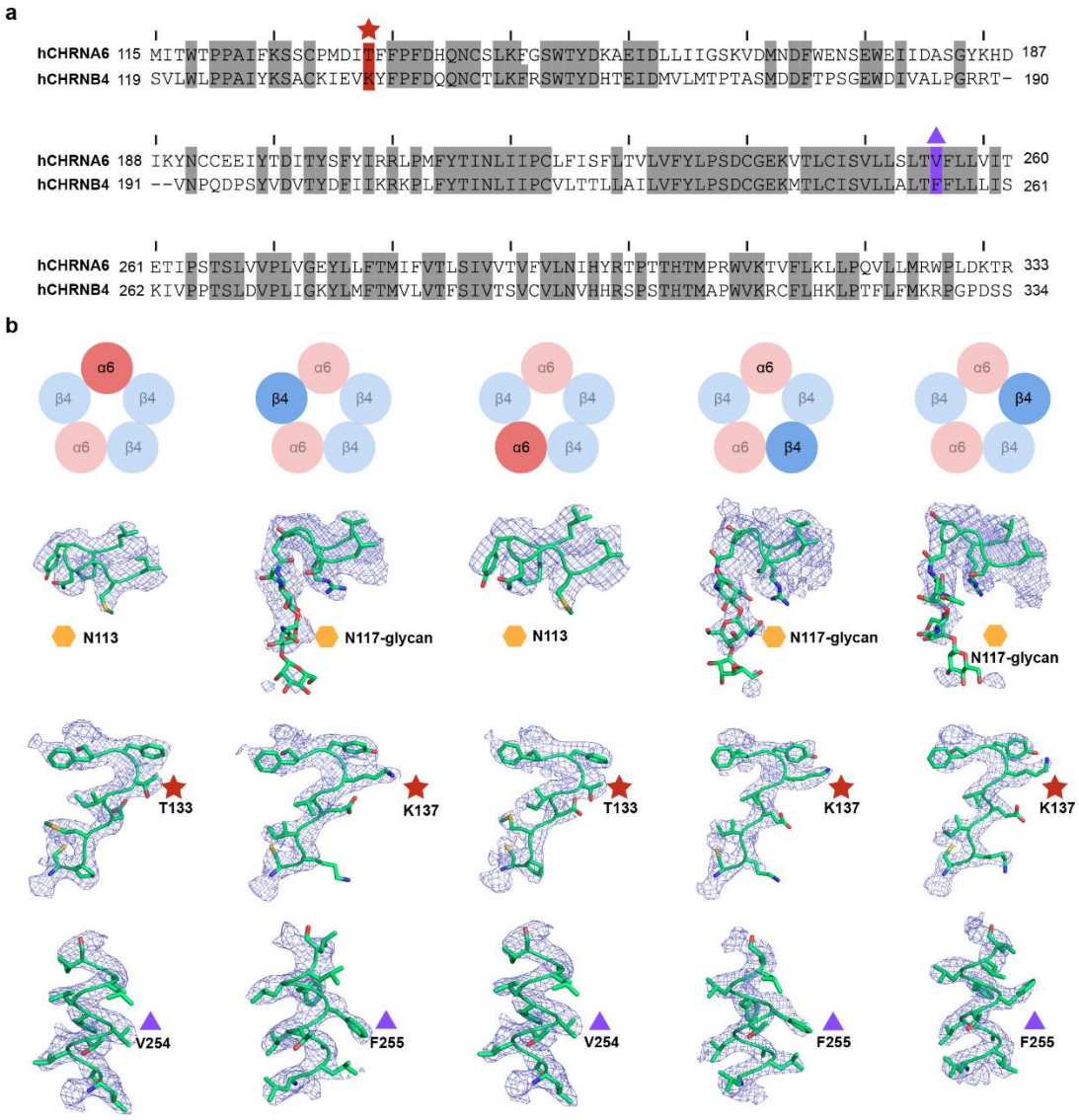


Supplementary Fig 4. The subunit stoichiometry of α6β4 receptor

**a.** A portion of sequence alignment of WT α6 and β4 subunits. Three non-conserved amino acids are highlighted in red, yellow and purple, respectively. **b.** The model diagram of subunit stoichiometry α6β4 receptor is represented by cycles. The α6 and β4 subunits are colored in burgundy and blue, respectively. The cryo-EM densities and atomic models of N-Glycan and non-conserved amino acids in two α6 and three β4 subunits. All structural information comes from the structure of α6β4 receptor bound with nicotine.

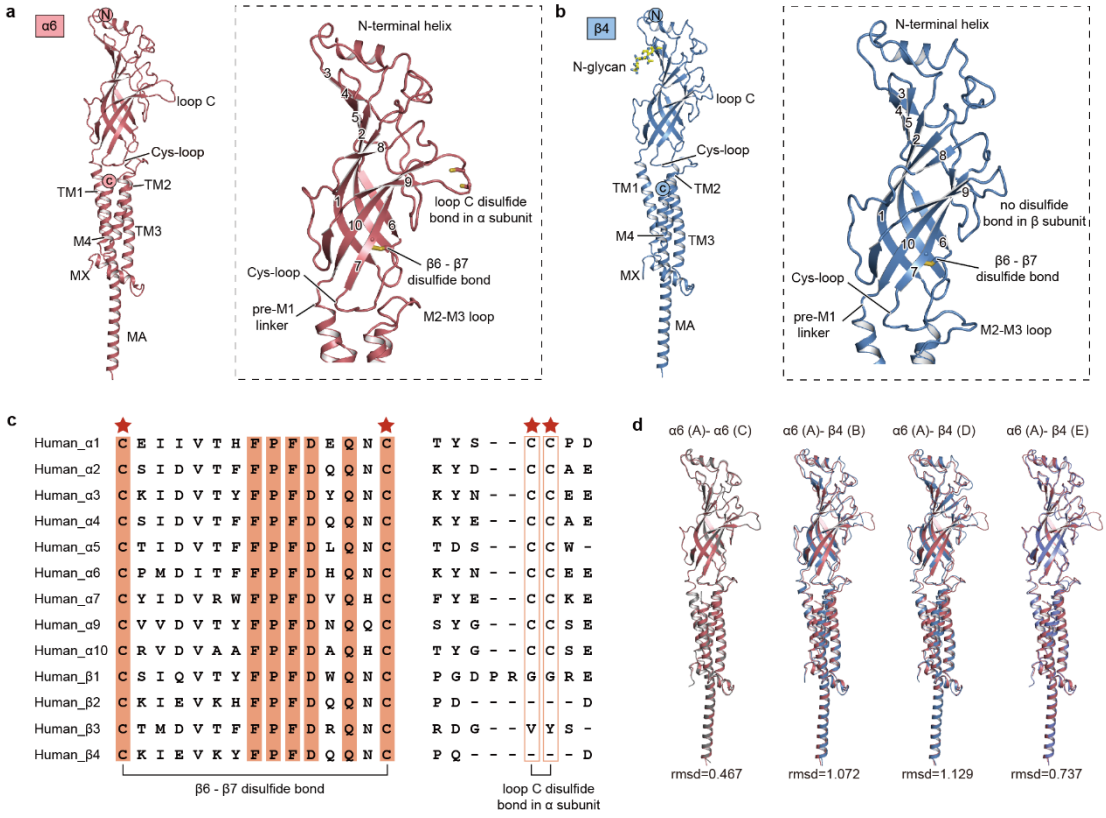


## Supplementary Fig 5. Comparison of the α6 and β4 subunits in the α6β4$^{nico}$ structure

**a-b.** The individual subunits of α6 (burgundy) and β4 (blue). The N-glycosylation in β4 is shown as yellow sticks and marked by black dashes. **c.** Sequence alignment of disulfide bonds within β6-β7 loop and loop C between all subunits of nicotinic receptors. The cystines are marked by red triangles. **d.** Backbone comparison of the α6 (burgundy) and β4 (blue) subunits. Cα atom r. m. s. d. from superimpositions of α6 (chain A) with other subunits.

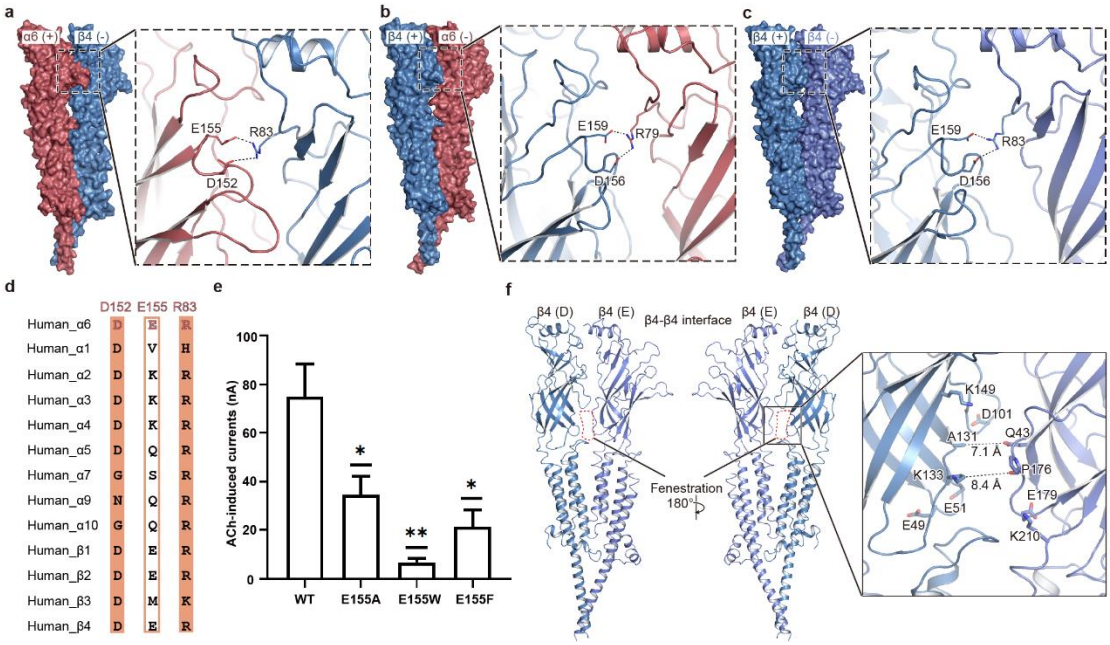


Supplementary Fig 6. Assembly of α6β4 receptor

**a-c.** The α6-β4, β4-α6, and β4-β4 interfaces are presented in surface and cartoon. The key residues for interaction are shown as sticks. The potential electrostatic interactions are presented as dashed lines. **d.** Sequence alignment of the conserved electrostatic interaction among α6-β4, β4-α6 and β4-β4 interfaces. **e.** ACh-induced currents of wild-type α6β4 receptor and its mutants in two-electrode voltage clamp experiment. Data represent the mean ± S.E.M. from three separate experiments. The ACh-induced currents of E155A, E155W and E155F are significantly lower than that of wild-type α6β4 receptor. $P < 0.05$ for all mutants, unpaired t-test. **f.** Extracellular fenestration unique to β4-β4 interface. Inset of fenestration with distance indicated by dashed lines. Side chain surrounding fenestration are shown as sticks.

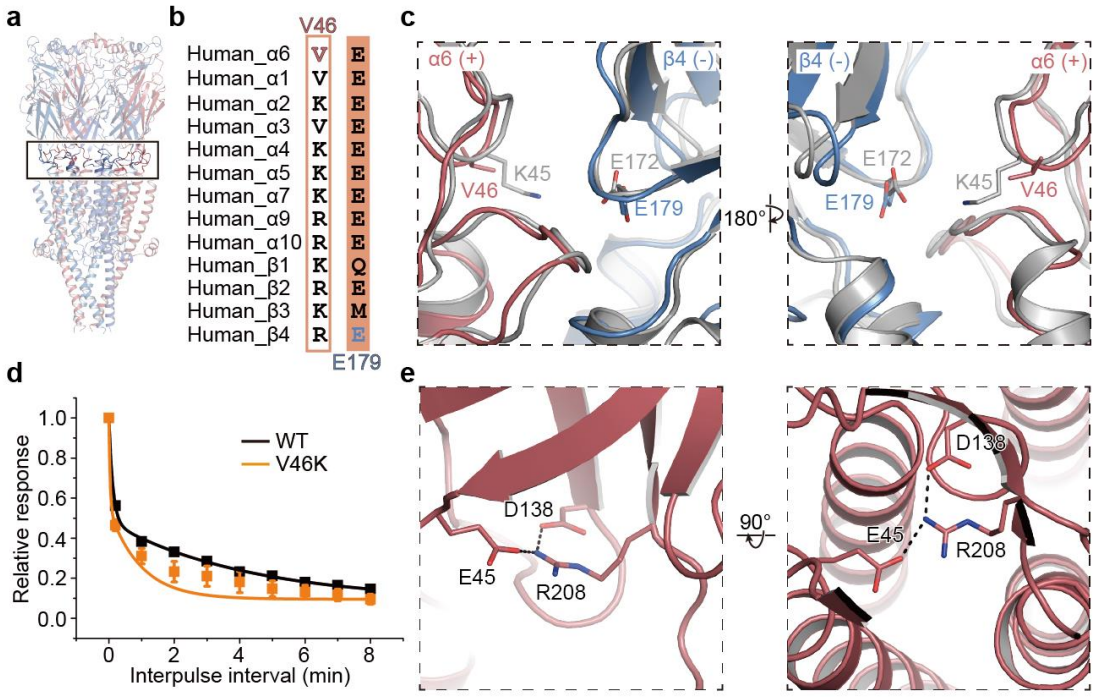


Supplementary Fig 7. The coupling region of α6β4 receptor

**a.** The coupling region in α6β4 receptor. **b.** Sequence alignment of the residues in couple region of α6β4 among nAChRs (left). Comparison of residues in the coupling region between α6β4 and α7 (right). **c.** The conserved residues in the coupling region of α6 subunit, viewed in parallel (left) and perpendicular (right) to the membrane. The potential interactions are presented as dashed lines. **d.** The desensitization rates of wild-type α6β4 receptor and its mutant in two-electrode voltage clamp experiment. Time course of ACh response for wild-type α6β4 receptor and its mutant. Data represent the mean ± S.E.M. from three separate experiments. The black and orange curves represent $\alpha6\beta4^{WT}$ receptor and its mutant ($\alpha6\beta4^{V46K}$), respectively. $\alpha6\beta4^{WT}$: Tau values (fast) = 2.92, Tau values (slow) = 0.08; $\alpha6\beta4^{V46K}$: Tau values (fast) = 0.67, Tau values (slow) = 0.02. **e.** The coupling region of α6 subunit. The key residues for interaction are shown as sticks.

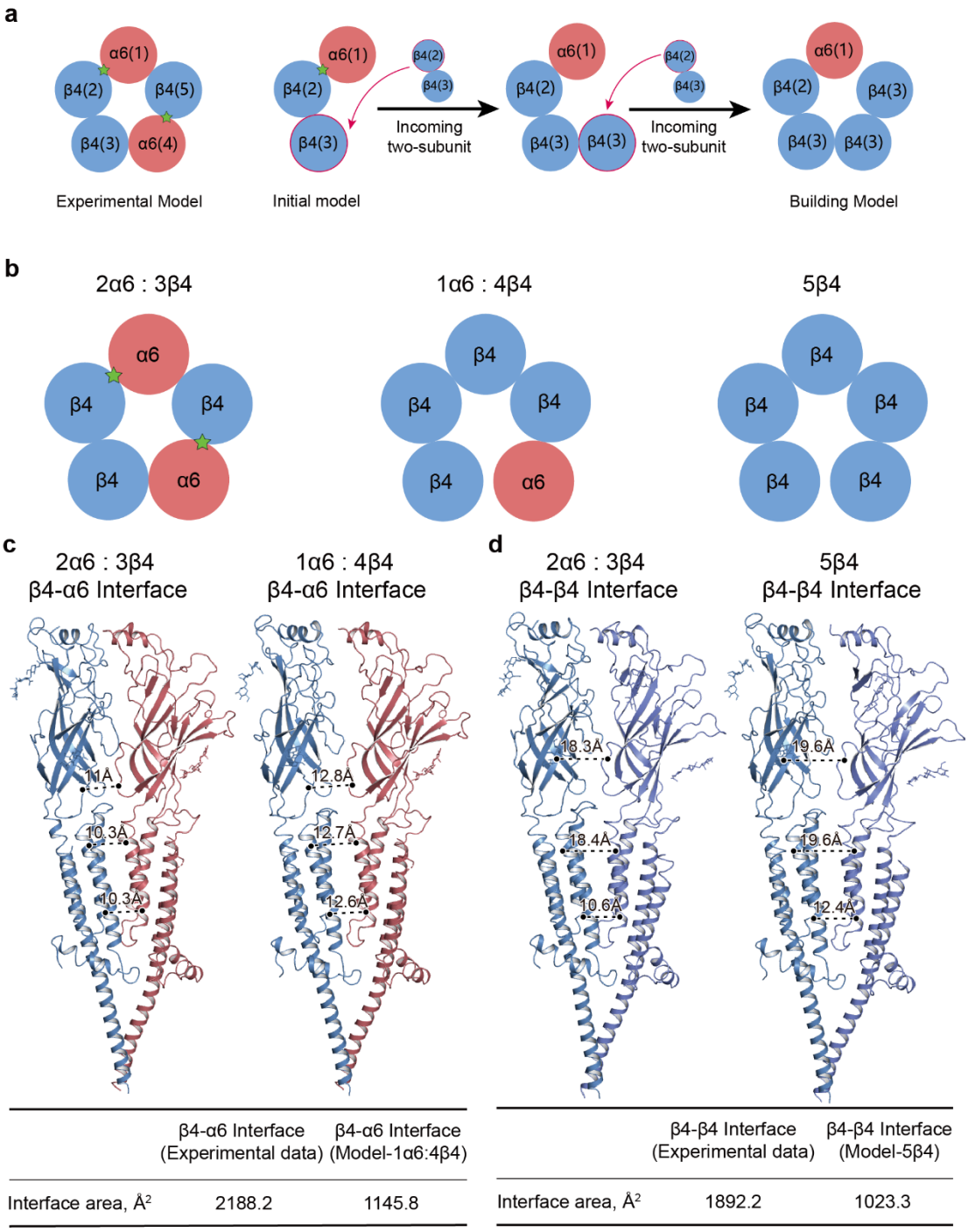


| | β4-α6 Interface (Experimental data) | β4-α6 Interface (Model-1α6:4β4) |
|---|---|---|
| Interface area, Å² | 2188.2 | 1145.8 |

| | β4-β4 Interface (Experimental data) | β4-β4 Interface (Model-5β4) |
|---|---|---|
| Interface area, Å² | 1892.2 | 1023.3 |

## Supplementary Fig 8. Theoretically possible pentamers of α6β4 receptor

**a.** To build the 1α6:4β4 receptor model, the α6 (4) subunit and β4 (5) subunit are removed from our experimental α6β4 structure, leaving one α6 subunit (α6 (1)) and two β4 subunits (β4 (2) and β4 (3)) as the initial model. Subsequently, the β4 subunits were added sequentially using a pairwise alignment approach. Specifically, during the addition of the fourth β4 subunit, the β4(3) subunit from the initial model was used as a structural reference and aligned with the β4(2) subunit of the incoming two-subunit. The fifth β4 subunit was then added in a similar manner, resulting in a model consisting of four β4 subunits and one α6 subunit. The 5β4 model was constructed using a similar stepwise

alignment process. After building these models, energy minimization was performed to optimize their structures. **b.** The model diagrams of subunit stoichiometry α6β4 receptor are represented by cycles. The α6 and β4 subunits are colored in burgundy and blue, respectively. The models of theoretical pentamers (5β4 and 1α6:4β4) based on our experimentally observed interfaces. **c-d.** The interfaces of experimental model (2α6:3β4) and theoretical models (5β4 and 1α6:4β4). Inset of interfaces with distances indicated by dashed lines. The values of interface buried surface areas between experimental model (2α6:3β4) and theoretical models (5β4 and 1α6:4β4) are shown in tables. Interfacial buried surface areas were calculated by PDBePISA server.

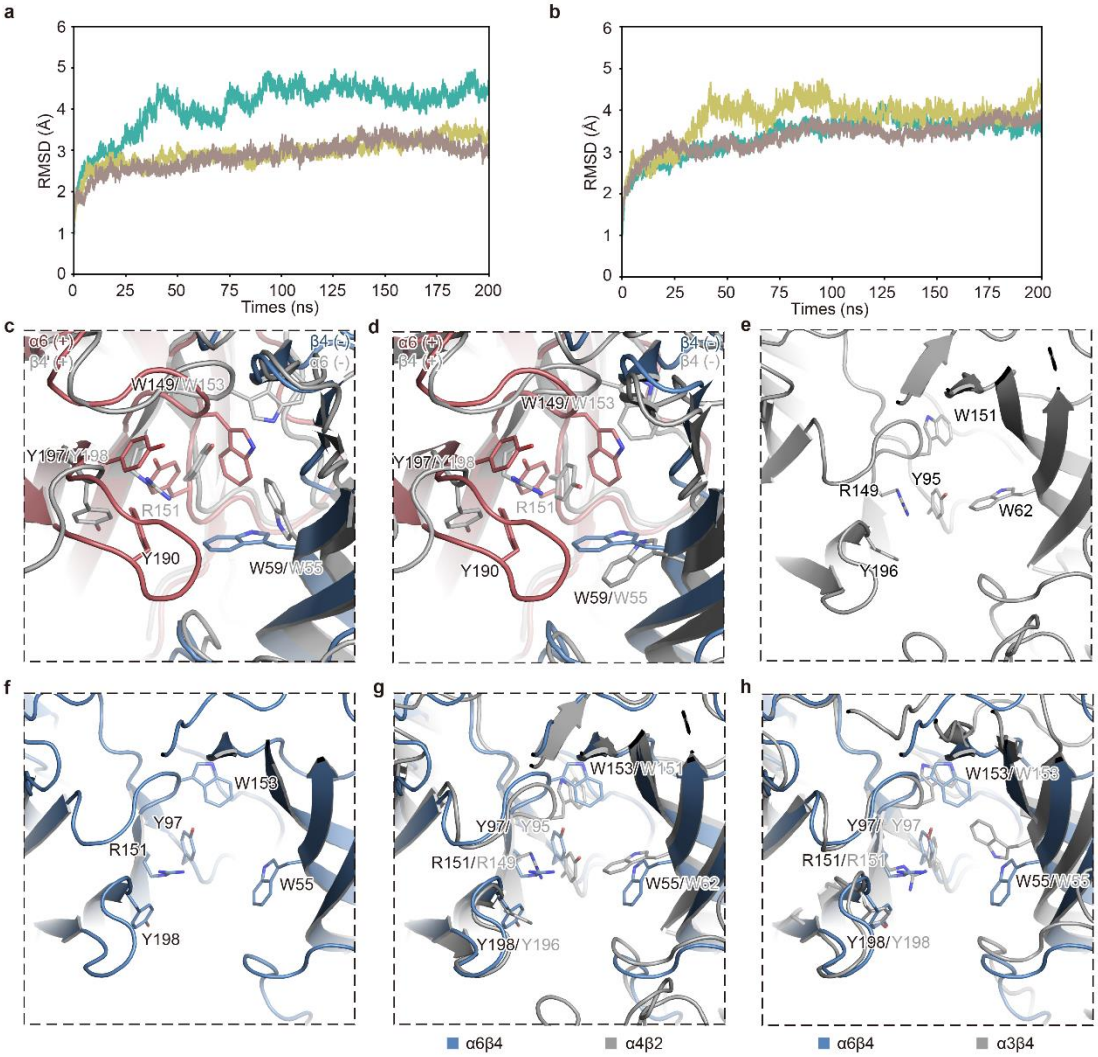


## Supplementary Fig 9. The binding pocket of nicotine

**a.** Heavy atom of R.M.S.D. of α6β4$^{nico}$ from the initial structure is plotted over time. Three simulations were performed for each simulation. **b.** Heavy atom of R.M.S.D. of α6β4$^{teb}$ from the initial structure is plotted over time. Three simulations were performed for each simulation. **c.** Comparison of nicotine binding pockets in α6-β4 and β4-α6 interfaces. The key residues are shown as sticks. **d.** Comparison of nicotine binding pockets in α6-β4 and β4-β4 interfaces. The key residues are shown as sticks. The nicotine is shown as sticks and spheres. **e.** The non-ligand binding site of α4β2 receptor. The key residues for interaction are shown as sticks. **f.** The non-ligand binding site of α6β4 receptor. The key residues are shown as sticks. **g.** Comparison of non-ligand binding site of α6β4 and α4β2. The key residues are shown as sticks. The α6β4 and α4β2 structures are colored in blue and gray, respectively. **h.** Comparison of non-ligand binding site of α6β4 and α3β4. The key residues are shown as sticks. The α6β4 and α3β4 structures are colored in blue and gray, respectively.

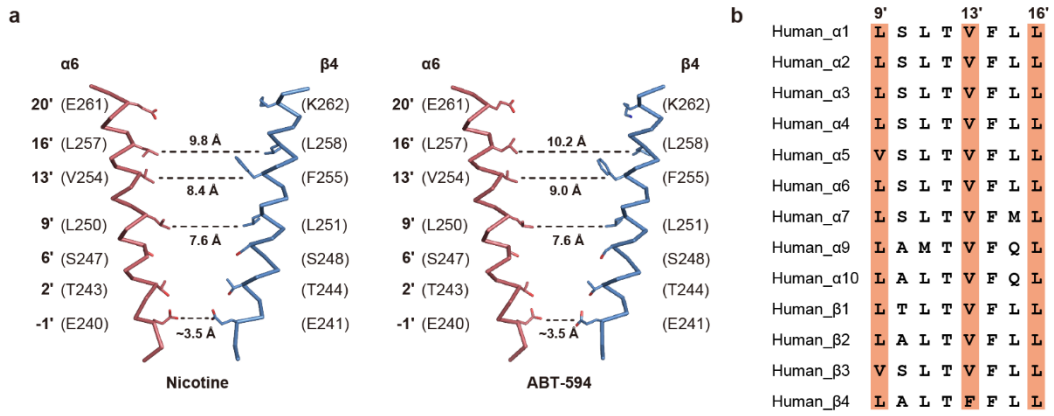


## Supplementary Fig 10. Ion permeation pathway and pore conformation

**a.** View of the M2 α-helices in α6β4$^{nico}$ from opposing subunits with side chains shown for pore-lining residues (left). View of the M2 α-helices in α6β4$^{teb}$ from opposing subunits with side chains shown for pore-lining residues (right). **b.** Sequence alignment of the conserved residues in the resting and desensitized gate among nAChRs.

Supplementary Table 1. Cryo-EM data collection, refinement and validation statistics.

| | α6β4$^{nico}$ (EMD-60401) (PDB 8ZRP) | α6β4$^{teb}$ (EMD-60400) (PDB 8ZRN) |
|---|---|---|
| **Data collection and processing** | | |
| Magnification | ×105,000 | ×105,000 |
| Voltage (kV) | 300 | 300 |
| Electron exposure (e$^{-}$/Å$^2$) | 60 | 60 |
| Defocus range (μm) | −1.2 – −2.2 | −1.2 – −2.2 |
| Pixel size (Å) | 0.85 | 0.85 |
| Symmetry imposed | C1 | C1 |
| Initial particle images (no.) | 2,228,791 | 3,256,486 |
| Final particle images (no.) | 40,331 | 39,153 |
| Map resolution (Å) | 3.3 | 3.2 |
| FSC threshold | 0.143 | 0.143 |
| **Refinement** | | |
| Model resolution (Å) | 3.5 | 3.5 |
| FSC threshold | 0.5 | 0.5 |
| Map sharpening *B* factor (Å$^2$) | -93.1 | -106.2 |
| Model composition | | |
| Non-hydrogen atoms | 16042 | 15997 |
| Protein residues | 1919 | 1913 |
| Ligands | 26 | 26 |
| *B* factors (Å$^2$) | | |
| Protein | 70.84 | 41.03 |
| Ligand | 102.42 | 75.07 |
| R.m.s. deviations | | |
| Bond lengths (Å) | 0.003 | 0.004 |
| Bond angles (°) | 0.545 | 0.594 |
| Validation | | |
| MolProbity score | 1.70 | 1.79 |
| Clash score | 5.50 | 5.65 |
| Poor rotamers (%) | 0.72 | 0.67 |
| Ramachandran plot | | |
| Favored (%) | 93.99 | 92.18 |
| Allowed (%) | 5.96 | 7.66 |
| Disallowed (%) | 0.05 | 0.16 |

Supplementary Table 2. System setup of MD simulation.

| **System** | Total number of atoms | Total number of water molecules | Salt concentration |
|---|---|---|---|
| $\alpha6\beta4^{nico}$ | 71851 | 13716 | 0.0451 M |
| $\alpha6\beta4^{teb}$ | 69788 | 13183 | 0.0474 M |